

# Deconvolution of Three-Component Teleseismic Data from Southern Tibet Using the SVA Technique

by Saptarshi Dasgupta, Robert L. Nowack, and Supriyo Mitra

**Abstract** In this study, the *SV* autocorrelation (SVA) technique of Dasgupta and Nowack (2006) is tested using three-component *P*-wave data from selected INDEPTH II and CDSN stations in southern Tibet. The SVA technique involves constructing an estimate of the source and distant Earth wavelet from the autocorrelation of the *SV* component and using this to deconvolve the data. The deconvolved vertical components are then used to infer the crustal *P*-velocity structure. Initial models for the inversion of the deconvolved vertical components were based on the *S*-velocity results obtained from the inversions of radial receiver functions by Mitra *et al.* (2005). The Moho depths obtained from inverting the vertical components deepen from the south to the north in the study area and are comparable to the depths obtained by Mitra *et al.* (2005) to the north and similar but somewhat shallower to the south. The crustal  $V_P/V_S$  ratios are obtained from the inverted  $V_S$  models from Mitra *et al.* (2005) and the inferred  $V_P$  speeds obtained from this study. Except for station BB18 with a somewhat higher  $V_P/V_S$  ratio, the other stations to the north in the Tethyan Himalayas and the southern Lhasa terrane have  $V_P/V_S$  ratios between 1.75 and 1.80 with a mean of 1.77 (a Poisson's ratio of 0.265). The range of values could result from noise in the data as well as from lateral heterogeneity in the region with different piercing points at depth for the *Ps* and *PpPp* phases.

## Introduction

In this study, the *SV* autocorrelation (SVA) technique of Dasgupta and Nowack (2006) is tested using teleseismic *P*-wave data from selected INDEPTH II and CDSN stations in southern Tibet. The deconvolved vertical components obtained from the SVA technique are then used to invert for the crustal *P*-velocity structure beneath these stations. The SVA technique involves constructing an estimate of the incident source and distant Earth wavelet from the *SV* component of the *P*-wave train, and then using it to deconvolve the three-component data. This assumes that the *P* to *SV* scattering coefficients beneath the receiver are random and white, and this is similar to the assumption made for *P* to *P* scattering for predictive deconvolution in exploration geophysics.

Systematic geological and geophysical investigations have been carried out across the Tibetan plateau over the past two decades and more recently in the Himalayas to understand the uplift, support, and deformation across this active tectonic collision zone between the Indian and Eurasian plates. An important effort has been the International Deep Profiling of Tibet and Himalayas (INDEPTH) project, which was carried out in three major phases. The INDEPTH II experiments produced a wealth of geophysical data across southern Tibet, which have been analyzed and interpreted by Nelson *et al.* (1996), Kind *et al.* (1996), Yuan *et al.*

(1997), and, more recently, by Mitra *et al.* (2005). These studies have provided seismic images of the crust and upper mantle beneath the Tibetan plateau.

Inversion of receiver functions and Rayleigh-wave phase velocities by Kind *et al.* (1996) yielded shear-wave velocity images of the crust and upper mantle beneath the Tibetan Plateau. The main observations of their study were a substantial south to north variation in the shear-wave velocity structure of the crust beneath southern Tibet and the presence of a low-velocity zone north of the Zangbo suture, which is absent further to the south beneath the Tethyan Himalayas.

Yuan *et al.* (1997) provided a detailed analysis of the earthquake data using receiver function analysis and demonstrated a northward deepening Moho beneath the southern Tibetan Plateau. Brown *et al.* (1996) observed anomalous amplitudes (bright spots) and negative polarity from seismic reflection profiling in the same region. These were interpreted as the presence of fluids (granitic magma or brines) in the middle crust beneath the Yadong–Gulu rift and possibly much of southern Tibet (Nelson *et al.*, 1996). This was also in agreement with an electrically conductive horizon at depths between 10 and 20 km north of the Himalayas (Chen *et al.*, 1996).

The seismic reflection profiles of Brown *et al.* (1996) also showed that the decollement beneath which the Indian lithosphere underthrusts the Himalayas extends about 225 km north of the Himalayan deformation front to a depth of about 50 km. Schulte-Pelkum *et al.* (2005) showed the presence of strong seismic anisotropy that developed above the decollement due to shear processes of earthquakes at shallower depths.

Mitra *et al.* (2005) performed receiver function profiling from northeast India and extending to southern Tibet (using the INDEPTH II data in southern Tibet) and were able to extend the decollement further south into the Lesser Himalayas at a depth of about 8 km. They imaged the geometry of the Indian Moho from the undeformed Indian shield beneath the Brahmaputra Valley to its underthrusting of the Himalayas. This showed that the Indian shield crust just south of the Himalayas is similar (in average shear velocity and thickness) to what is seen in southern India (Rai *et al.*, 2003) and that the Moho progressively deepens as the Indian lithospheric plate underthrusts the Himalayas and southern Tibet due to crustal doubling.

Chen and Yang (2004) used high-resolution seismic waveform modeling to show that some earthquakes occurred in the mantle portion of the lithosphere greater than 100 km in depth suggesting that the mantle lithosphere is strong enough to accumulate elastic strain. Monslave *et al.* (2006) presented a bimodal depth distribution for earthquakes in the Himalayas of eastern Nepal and the southern Tibetan Plateau. They indicated that clusters of earthquakes form well-defined zones of seismicity at depths between 50 and 100 km suggesting the presence of earthquakes at sub-Moho depths. Also, Zhu and Helmberger (1996) showed the existence of intermediate depth earthquakes in the mantle lithosphere in this area by modeling broadband waveforms recorded on a temporary PASSCAL array.

In contrast, Jackson (2002) inferred that earthquakes in southern Tibet were in the crust suggesting the existence of a single seismogenic layer. Mitra *et al.* (2005) modeled depths and focal mechanisms of recent moderate-to-large earthquakes from northeast India and eastern Himalaya using *P*- and *SH*-waveform inversions. They recomputed depths of earthquakes analyzed by other workers from the region (e.g., Chen and Molnar, 1990, Zhu and Helmberger, 1996, see also table A1 from Mitra *et al.*, 2005) using the receiver function derived shear-wave velocity models obtained from their study. The depth distribution of these relocated earthquakes pointed to a single seismogenic layer comprising a strong Indian shield crust.

Chen and Molnar (1981) used group and phase velocity dispersion of Rayleigh waves along with regional *P*-wave phases to model the structure of the crust and upper mantle under Tibet with results indicating the thickness of the crust to be around 65–80 km. Sun and Toksoz (2006) used tomographic methods to develop a 3D *P*-wave velocity model for the crust and the uppermost mantle of China and surrounding areas. The area around Tibet had higher average *P*-wave

crustal velocities due to thickening of the crust. Li and Mooney (1997), Hearn *et al.* (2004), and Li *et al.* (2006) had similar results indicating higher *P*-wave crustal velocities due to the northward injection of the cold Indian plate in southern Tibet, which is absent in northern Tibet. Also, Liang and Song (2006) proposed *Pn* velocity variations of the Tibetan Plateau and its neighboring regions using refraction tomography.

Using shear-couple teleseismic *P*-waves from the 1991–1992 Tibetan Plateau experiment, Owens and Zandt (1997) found for station SANG in the central Lhasa terrane an average crustal  $V_P/V_S$  of 1.78 (a Poisson's ratio of 0.27), which is near the global average for the continental crust (Zandt and Ammon, 1995; Christensen, 1996). Modeling regional *Pnl* waveforms, Rodgers and Schwarz (1997) inferred a Poisson's ratio of  $0.25 \pm 0.02$  for the stations LHASA and SANG in the Lhasa terrane. Integrating receiver function data from a number of international experiments including INDEPTH II and III, Kind *et al.* (2002) determined a varying crustal  $V_P/V_S$  along their profiles. From their figure 3, for north latitudes between 29 and 30.5° in the Tethyan Himalayas and the southern Lhasa terrane the values of  $V_P/V_S$  vary around 1.75 (with the Poisson ratios varying around 0.26). However, they infer locally higher values of  $V_P/V_S$  between 30.5 and 32° north latitude on their east line and 32 and 34° north latitude on their west line. Kind *et al.* (2002) concludes that even though magma or fluid in the Tibetan crust is great enough to enhance electrical conductivity, it may not be great enough to elevate average crustal  $V_P/V_S$ , except locally along active Tibetan rifts.

### The SVA Technique

Teleseismic *P*-wave data can be modeled as the convolution of the *P*-wave signature from the source and distant earth structure with scattering coefficients from the receiver crust and upper mantle. In the SVA approach of Dasgupta and Nowack (2006), the *P* to *SV* scattering coefficients from the structure beneath the receiver are assumed to be random and white. By rotating the components and using a free surface correction, the *SV* component is obtained that removes the direct *P* wave from this component. The autocorrelation of the *SV* component is used to provide an estimate of the autocorrelation of the incident source and distant Earth wavelet. This approach is similar to the use of the autocorrelation of a reflection seismogram to estimate the source function in exploration seismology where the *P* to *P* scattering coefficients are assumed to be random and white (Webster, 1978; Robinson and Osman, 1996). For the teleseismic case, the SVA can be used to deconvolve the processed, unrotated vertical and horizontal components of the seismic data.

To form the complete source wavelet from the autocorrelation and its corresponding power spectrum, knowledge of the phase spectrum is necessary. For a minimum phase signal, the log of the power spectrum and the phase spectrum form a Hilbert transform pair (Oppenheim and Schaffer,

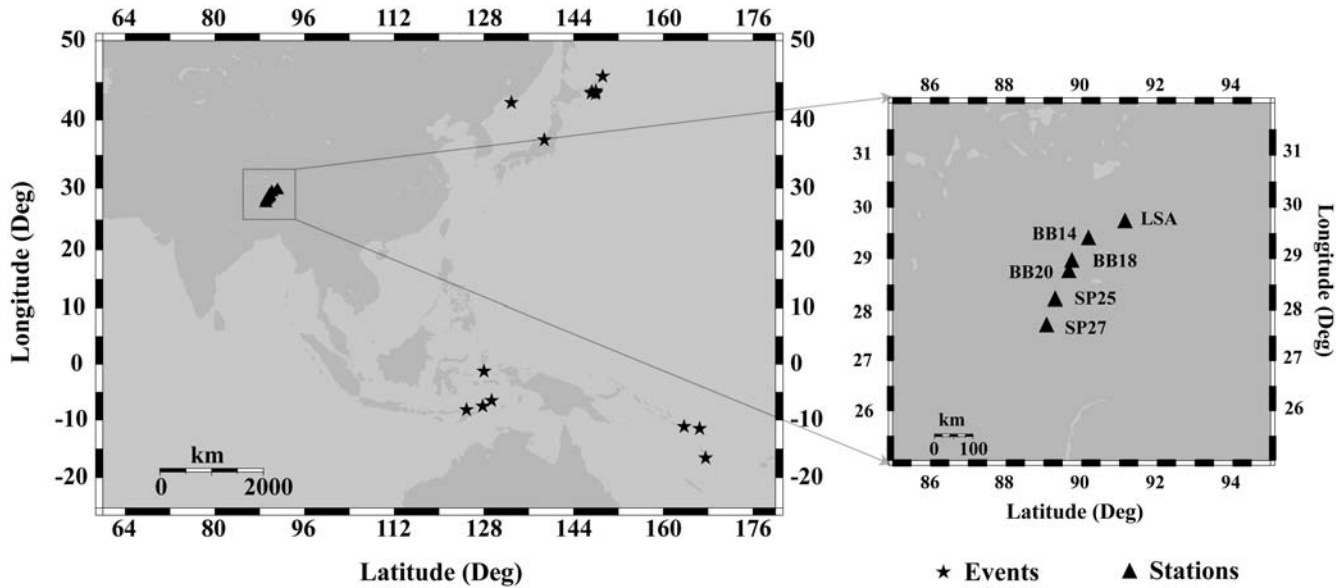


**Figure 1.** Location of the stations and teleseismic events in this study. The black triangles are the stations used in this study from the INDEPTH II experiment, and the stars represent the teleseismic events that were processed in this article.

1975). We can therefore construct a minimum phase source wavelet from the power spectrum and use it for the deconvolution. But, an earthquake source wavelet is not in general minimum phase. However, the original seismic data can be processed to be minimum phase (Bostock, 2004) and these processed data including the vertical component can be deconvolved with the estimated minimum phase source wavelet from the SVA function. A further overview of the method is given in the Appendix and a more detailed description with examples is given by Dasgupta and Nowack (2006). We apply and test this approach for the deconvolution of the vertical component *P*-wave data for stations in southern Tibet.

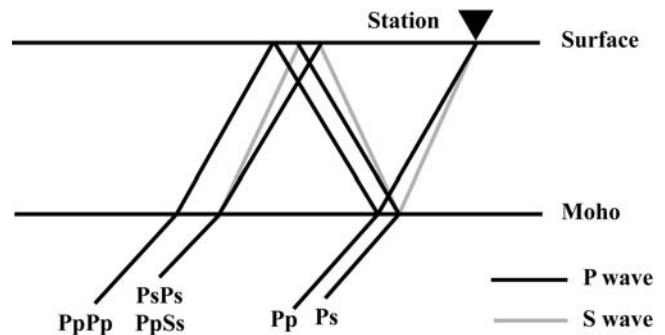
### Inversion for *P*-Velocity Crustal Structure in Southern Tibet

The locations of the stations from INDEPTH II and CDSN used in this study are shown in Figure 1 with triangles from the crest of the Himalayas north for approximately 300 km to the center of the Lhasa block. The teleseismic events used in this study are represented as stars in this figure. The locations of the events are mostly in the eastern quadrant because the structure that we are trying to image is towards the east of the stations. A wider distribution of azimuth would lead to different piercing points for the rays and would average out the structure in the stacks. Mitra *et al.* (2005) performed receiver function analysis to study the *S*-wave structure and Moho geometry beneath these stations. Their inversion results are used to obtain initial *P*-velocity models for the inversions of the deconvolved vertical seismic data assuming an initial Poisson solid. Figure 2 shows the ray paths of the scattered and reflected phases from an incident teleseismic *P* wave. The black lines represent *P* phases and the gray lines represent converted *S* phases. For this study,

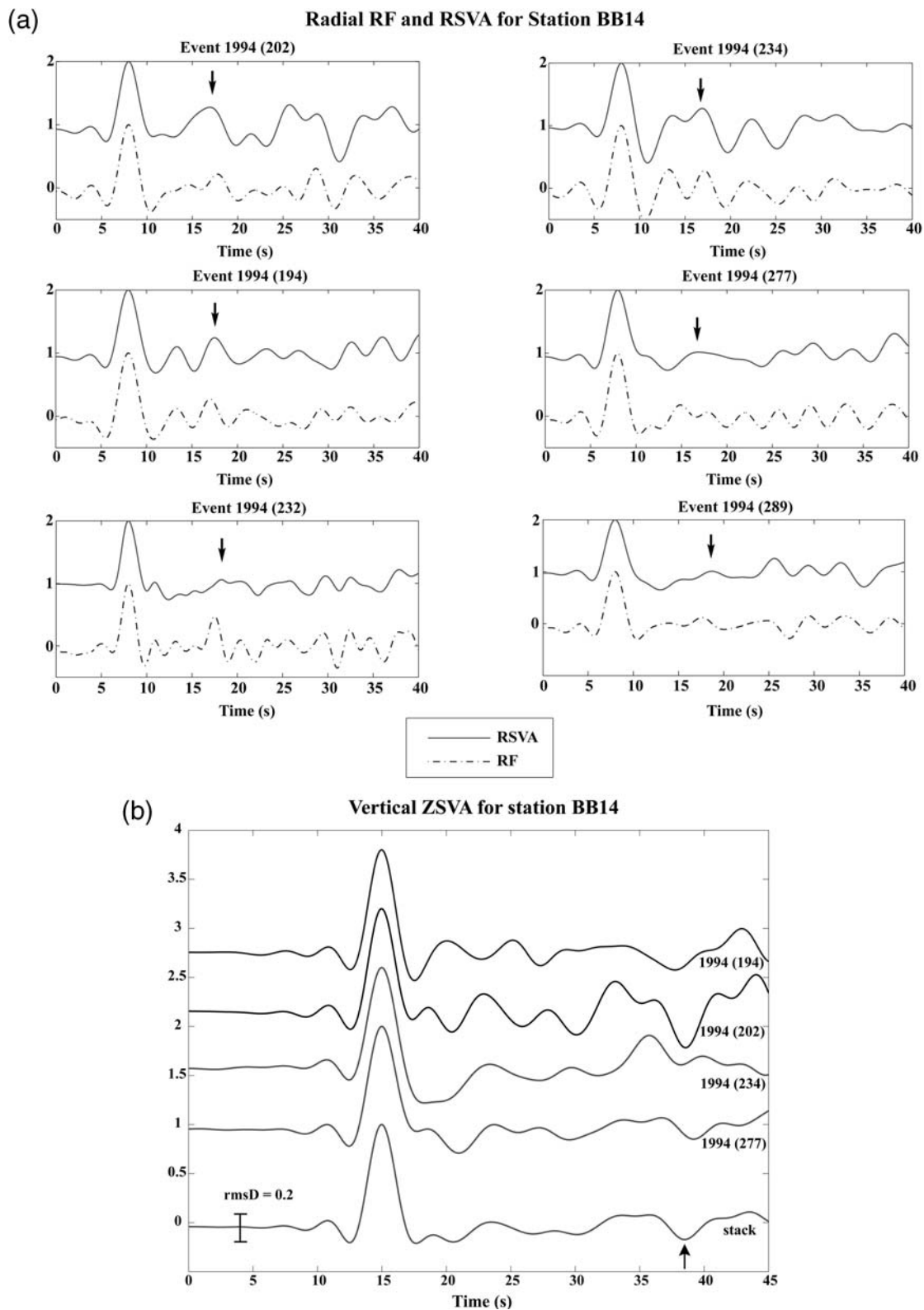
we are interested in imaging the *PpPp* phases on the selected stations, in particular the *PpPmp* phase for the Moho.

Figure 3a compares the radial receiver functions obtained from the SVA technique (solid curve) and that using the receiver function processing of Ammon *et al.* (1990) (dash-dotted curve) for events recorded at station BB14 used by Mitra *et al.* (2005). The vertical arrows indicate the approximate locations of the *Ps* phase arrival from the Moho. Based on these comparisons of the radial components using the two techniques, a subset of the deconvolved vertical components using the SVA approach was selected for further processing. About 60% of the events recorded at various stations were selected with this methodology and used to obtain the vertical component stack for further processing.

Figure 3b shows the stack of the deconvolved vertical components obtained from the selected events on station



**Figure 2.** The ray path nomenclatures for various conversions are shown in this figure. The horizontal lines represent the surface and the Moho from the top. The inclined black lines are the *P*-wave travel paths, and the inclined gray lines are the *S*-wave travel paths. In this article, we applied the SVA approach to constrain the *PpPp* phases on the deconvolved vertical components of the teleseismic recordings.



**Figure 3.** (a) Comparison of the radial receiver functions obtained from the SVA technique (solid curve) and that using receiver function processing of Ammon (1990) (dash-dotted curve) for events recorded at station BB14 used by Mitra *et al.* (2005). The vertical arrows indicate the approximate location of the  $P_s$  phase arrival for the Moho. Based on these comparisons a subset of deconvolved vertical components using the SVA approach was selected for further processing. (b). A stack of the deconvolved vertical components for station BB14. Based on the comparison of the radial receiver functions in (a), a subset of deconvolved vertical components was selected for stacking. The arrow on the stack indicates the approximate location of the  $PpPmp$  phase for station BB14. The error bar on the stack denotes the approximate error resulting from the stack.

BB14. The arrow on the stack in Figure 3b indicates the approximate location of the *PpPmp* phase for station BB14. The error bar denotes the approximate data error as obtained from stacking the event data.

A synthetic test is first performed to test the inversion of the deconvolved vertical components for *P*-wave crustal structure. The Bayesian approach of Tarantola (1987, 2005) was used for the inversions. Figure 4a shows the true model used to generate the observed vertical component data shown by the solid line. Noise is added to the synthetic data at a level of 1% with respect to the incident *P* arrival. However, this noise level is higher with respect to the amplitude of the scattered phases. The dash-dotted line with the error bars is the starting velocity model for performing the inversion. The final model is shown as a dashed line with the final error bars

now less than the line thickness and almost overlays the true model. Figure 4b shows the mismatch in the timing of the phases that exists between the calculated seismogram for the starting model and the observed data for the true model. The error bar indicates the approximate data error assumed for the observed data, and the data residual between the two seismograms is shown as a dotted curve. The arrow indicates the approximate location of the *PpPmp* phase on the observed data. Figure 4c shows the calculated seismogram (dashed curve) for the final model after two iterations. It can be seen that the data residual is significantly reduced in Figure 4b, which is evident from the match for the timing of the *PpPmp* phase. Also, the final model is shown in Figure 4a and has converged with the true model for the observed data.

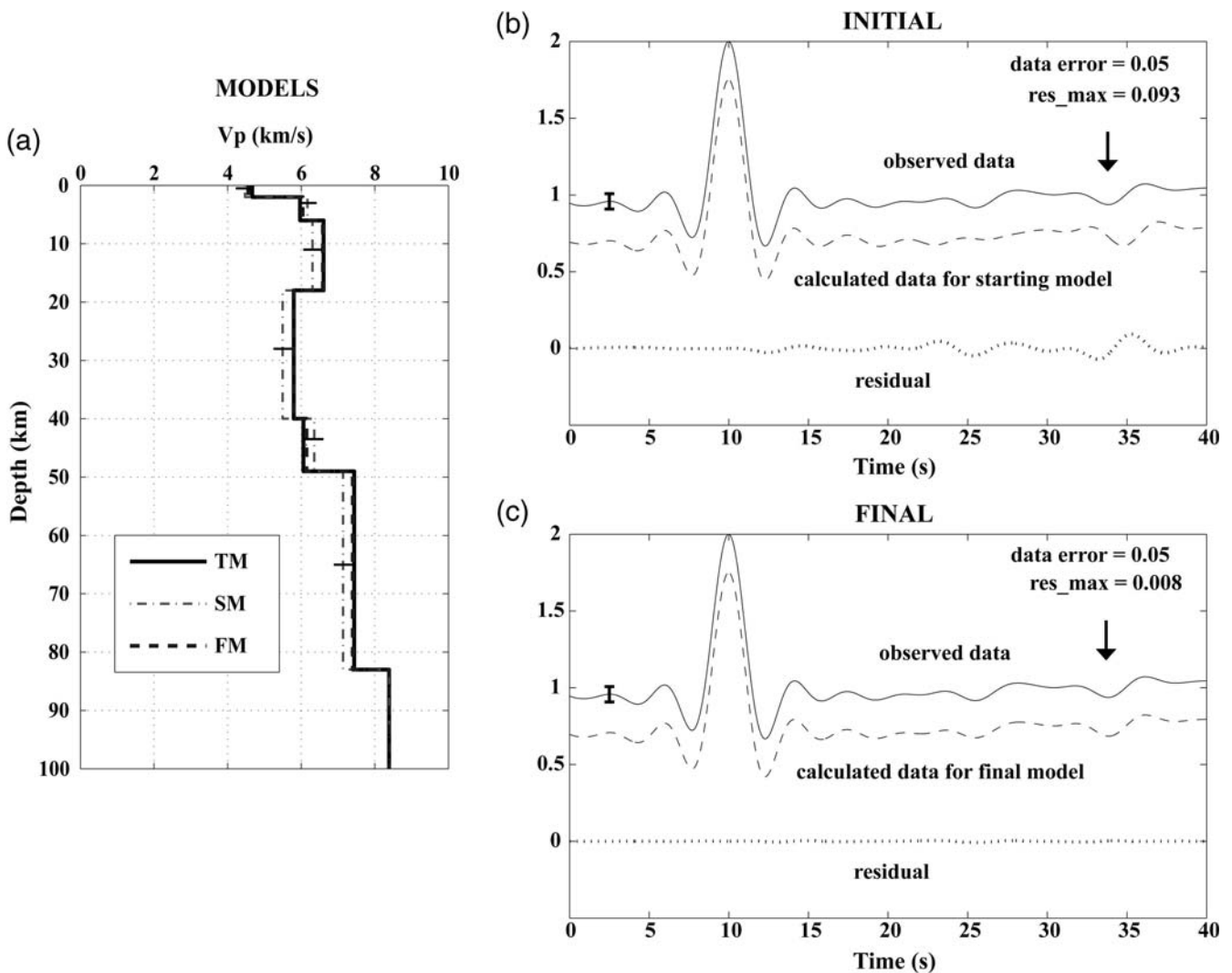
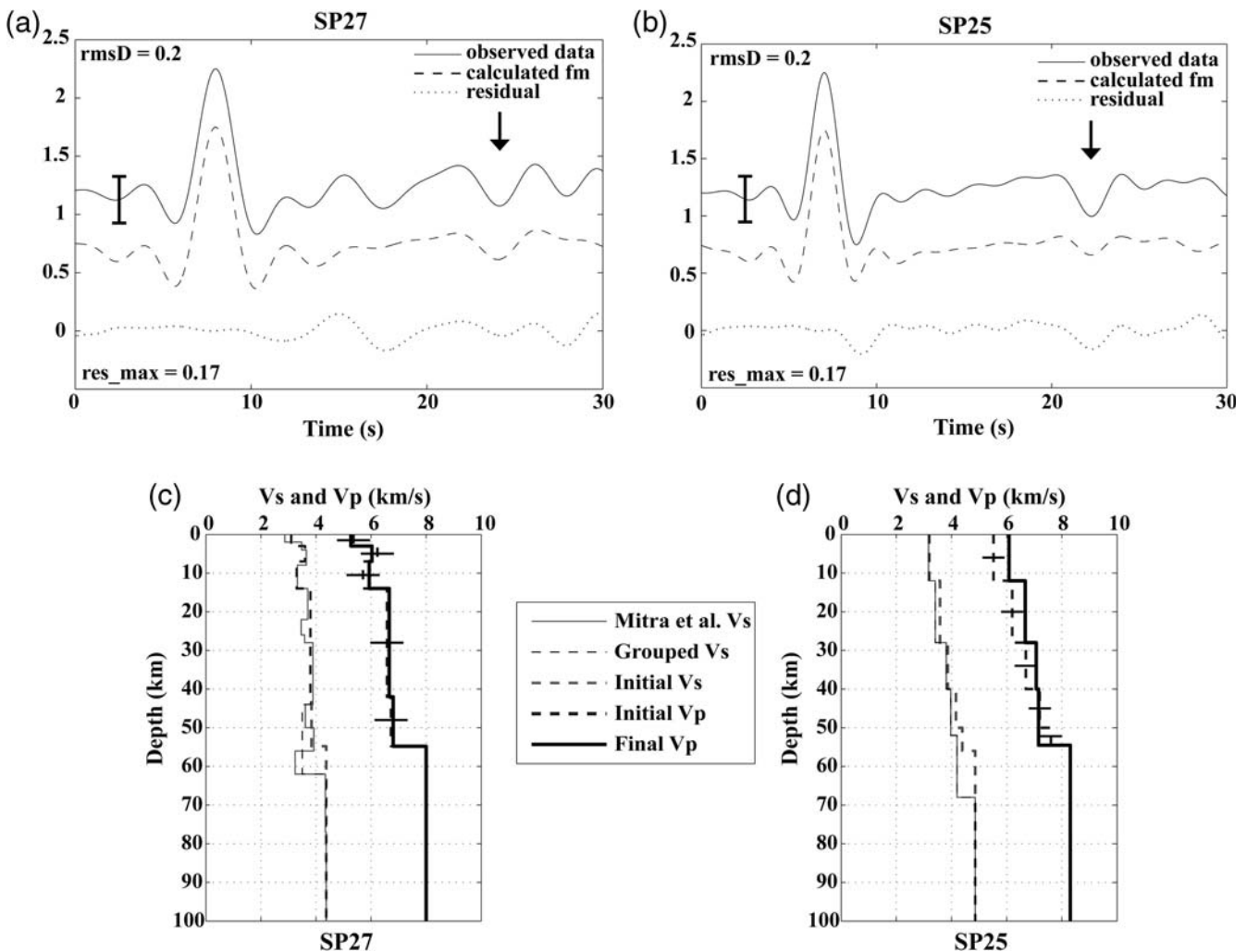


**Figure 4.** (a) The true velocity model (TM, solid line), the starting model (SM, dash-dotted line), and the final model (FM, dashed line) are shown. Prior model errors are shown. The final model errors are within a line width. (b) The observed data (solid curve) from the true model with added noise and the synthetic data (dashed curve) calculated for the starting model showing the initial data residual as the dotted line. The error bar shows the assumed data error, and the arrow shows the timing of the *PpPmp* phase. (c) The observed data (solid curve) and the calculated data (dashed curve) for the final model are shown. The dotted curve is again the data residual, which has been significantly reduced as compared to the initial data residual in (b). The arrow indicates the timing of the *PpPmp* phase on the observed data, which now matches very well with the synthetic seismogram calculated with the final velocity model.

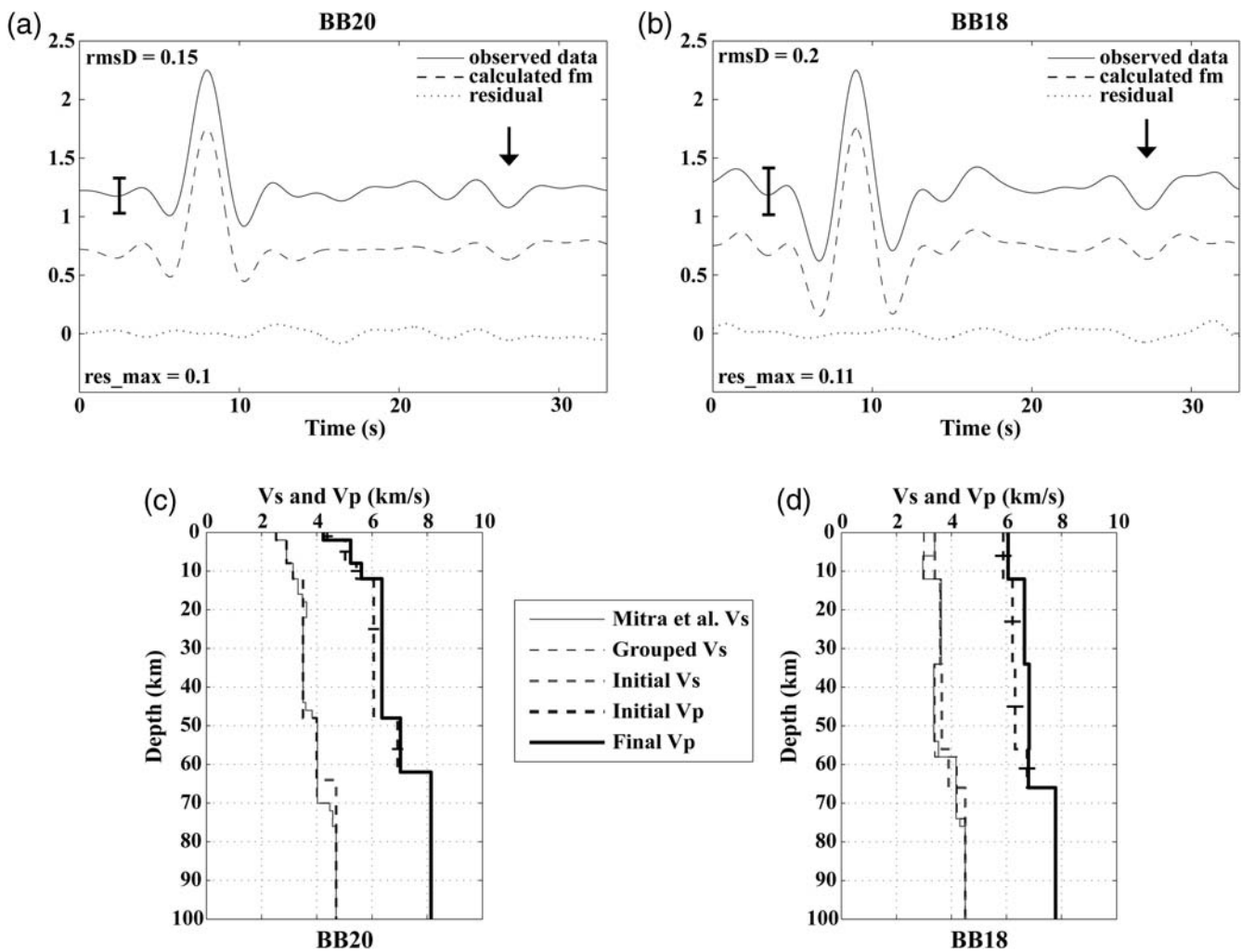
For the observed data in southern Tibet, we start with the  $V_S$  model of Mitra *et al.* (2005) shown by the thin solid lines for the  $V_S$  models in subplots (c) and (d) of Figures 5–7. The  $V_S$  layers were then grouped to form simple layers and denoted by a thin dashed line for the  $V_S$  in subplots (c) and (d) of Figures 5–7. These grouped  $V_S$  velocities were converted to a starting  $V_P$  model by assuming an initial Poisson solid. First order forward modeling was then performed to approximately align the  $PpPmp$  phase for the Moho. The resulting thick dashed lines for both  $V_P$  and  $V_S$  were then used as the starting models for the inversions.

Figure 5a,b show the stacked, deconvolved vertical component data (solid curves) for the southern stations SP27 and SP25 in Figure 1. Although these are short period stations, the  $PpPmp$  phases can be identified and are shown by

the arrows. The approximate data error based on the noise levels before the direct  $P$  arrival on the stacks is indicated by the error bars. Although the errors bars are large, the locations of the  $PpPmp$  arrivals as indicated by the arrows can be clearly seen on all stations. The dashed curves are the calculated seismograms for the final  $V_P$  velocity models for stations SP27 and SP25 shown in Figure 5c,d, respectively, and the dotted curves are the data residuals. The thin solid lines in Figure 5c,d are the initial  $V_S$  models for the stations SP27 and SP25 obtained from Mitra *et al.* (2005), which have been combined into simpler models represented by thin dashed lines. The thick dashed lines represent the starting  $V_P$  velocity model, as well as the starting  $V_S$  model. Again, the starting  $V_P$  model is obtained by converting the starting  $V_S$  model to the  $V_P$  model by assuming an initial Poisson



**Figure 5.** (a) and (b) The stacked deconvolved vertical seismic data (solid curve) for stations SP27 and SP25. The arrows indicate the timing of the approximate  $PpPmp$  phase for these stations. The approximate data error from the stacks is indicated with the error bars. The dashed curves are the calculated seismograms for the final  $V_P$  models for SP27 and SP25, shown in (c) and (d), respectively. The dotted curves are the data residuals. (c) and (d) The thin solid lines are the initial  $V_S$  models for the stations SP27 and SP25 obtained from Mitra *et al.* (2005). The thin dashed lines are simpler models (grouped  $V_S$ ) obtained from the initial  $V_S$  models. The thick dashed lines represent the starting  $V_S$  model, as well as the starting  $V_P$  model for the inversions. Error bars denote the starting model uncertainties. The starting  $V_P$  model is obtained by converting the starting  $V_S$  model to the  $V_P$  model using a ratio of 1.73 and subsequently adjusting the Moho depth with initial forward modeling of the  $PpPmp$  phase. The thick solid lines are the final  $V_P$  models obtained after inversions.



**Figure 6.** (a) and (b) The stacked deconvolved vertical seismic data (solid curves) for stations BB20 and BB18. The arrows indicate the timing of the approximate *PpPmp* phase for these stations. The approximate data error from the stacks is indicated with the error bars. The dashed curves are the calculated seismograms for the final  $V_P$  models for BB20 and BB18, shown in (c) and (d), respectively. The dotted curves are the data residuals. (c) and (d) The thin solid lines are the initial  $V_S$  models for the stations BB20 and BB18 obtained from Mitra *et al.* (2005). The thin dashed lines are simpler models (grouped  $V_S$ ) obtained from the initial  $V_S$  models. The thick dashed lines represent the starting  $V_S$  model, as well as the starting  $V_P$  model for the inversions. Error bars denote the starting model uncertainties. The starting  $V_P$  model is obtained by converting the starting  $V_S$  model to the  $V_P$  model using a ratio of 1.73 and subsequently adjusting the Moho depth with initial forward modeling of the *PpPmp* phase. The thick solid lines are the final  $V_P$  models obtained after inversions.

solid and subsequently adjusting the Moho depth with a forward modeling of the *PpPmp* phase for the observed data. The error bars denote the starting model uncertainties. The final  $V_P$  models are represented by thick solid lines and are obtained by inverting the stacked vertical seismograms using a Bayesian inversion approach, which has been previously validated with synthetic data in Figure 4. Although the formal uncertainties in the final model from these inversions are small, the actual uncertainties are larger because of non-uniqueness and lateral variability of the velocity structure. Assuming an uncertainty in the picking of the *PpPmp* phase of  $\pm 1$  sec and a crustal thickness of 65 km and speed of 6.4 km/sec would result in an uncertainty of the Moho depth of  $\pm 3$  km or an average crustal velocity uncertainty of  $\pm 0.3$  km/sec.

Similar processing has been done for stations BB20, BB18, and BB14 from the INDEPTH II stations and the station LSA from CDSN located in Figure 1. Figure 6 shows the results for stations BB20 and BB18. Figure 6a,b shows the stacked, deconvolved vertical components (solid curve). The arrows indicate the approximate location of the *PpPmp* phase and the data error from the stacks is indicated by the error bars. The dashed curves are the calculated seismograms for the final  $V_P$  velocity models for stations BB20 and BB18 shown by Figure 6c,d, respectively, and the dotted curves are the data residuals. The thick dashed lines represent the starting  $V_P$  velocity model, as well as the starting  $V_S$  model. Again, the starting  $V_P$  model is obtained by converting the starting  $V_S$  model to the  $V_P$  model by assuming an initial Poisson solid and subsequently adjusting the Moho depth

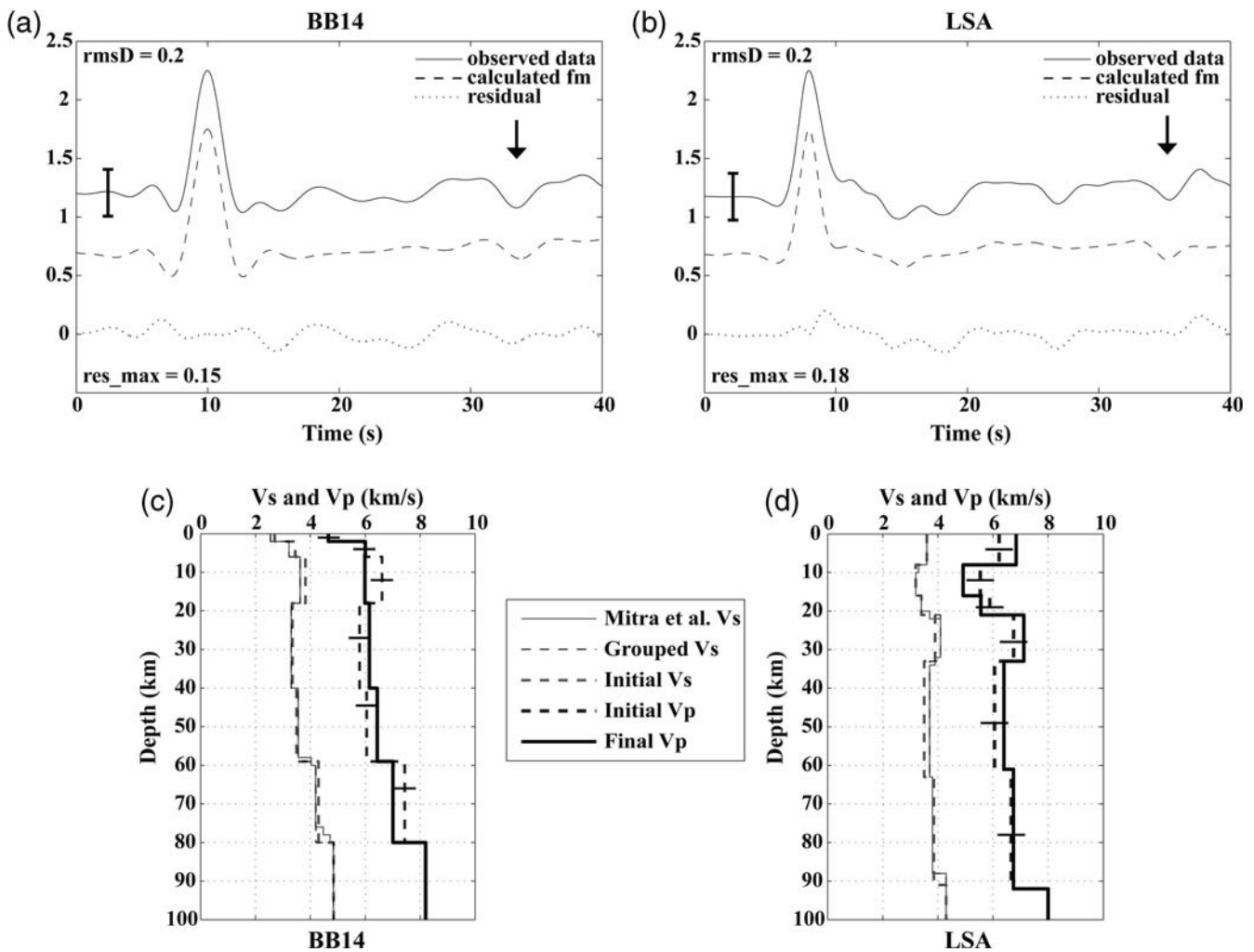


**Figure 7.** (a) and (b) The stacked deconvolved vertical seismic data (solid curves) for stations BB14 and LSA. The arrows indicate the timing of the approximate  $PpPmp$  phase for these stations. The approximate data error from the stacks is indicated with the error bars. The dashed curves are the calculated seismograms for the final  $V_P$  models for BB14 and LSA, shown in (c) and (d), respectively. The dotted curves are the data residuals. (c) and (d) The thin solid lines are the initial  $V_S$  models for the stations BB14 and LSA obtained from Mitra *et al.* (2005). The thin dashed lines are simpler models (grouped  $V_S$ ) obtained from the initial  $V_S$  models. The thick dashed lines represent the starting  $V_S$  model, as well as the starting  $V_P$  model for the inversions. Error bars denote the starting model uncertainties. The starting  $V_P$  model is obtained by converting the starting  $V_S$  model to the  $V_P$  model using a ratio of 1.73 and subsequently adjusting the Moho depth with initial forward modeling of the  $PpPmp$  phase. The thick solid lines are the final  $V_P$  models obtained after inversions.

with a forward modeling of the  $PpPmp$  phase for the observed data. The final  $V_P$  velocity models are represented by thick solid lines and are obtained by inverting the stacked vertical seismograms using a Bayesian inversion approach.

Figure 7 shows the results for stations BB14 and LSA. Figure 7a,b shows the stacked, deconvolved vertical components (solid curves) of stations BB14 and LSA located in Figure 1. The arrows indicate the approximate location of the  $PpPmp$  phase, and the data error from the stacks is indicated by the error bars. The dashed curves are the calculated seismograms for the final  $V_P$  models for stations BB20 and BB18 shown by Figure 7c,d, respectively, and the dotted curves are the data residuals. The thick dashed lines represent the starting  $V_P$  model, as well as the starting  $V_S$  model. As done previously in Figures 5 and 6, the starting  $V_P$  model

is obtained by converting the starting  $V_S$  model to the  $V_P$  model by assuming an initial Poisson solid and subsequently adjusting the Moho depth with a forward modeling of the  $PpPmp$  phase for the observed data. The final  $V_P$  velocity models are represented by thick solid lines and are obtained by inverting the stacked, vertical seismograms using a Bayesian inversion approach. Again formal uncertainties in the final model are small, but actual uncertainties are similar to the other stations.

Figure 8 shows a north–south profile of the southern Tibetan Plateau, which has been adapted from Mitra *et al.* (2005). It covers the distance from the station LSA in the north to the station SP27 in the south. It compares the Moho depths obtained from inverting the deconvolved vertical component data using the SVA technique in this study with

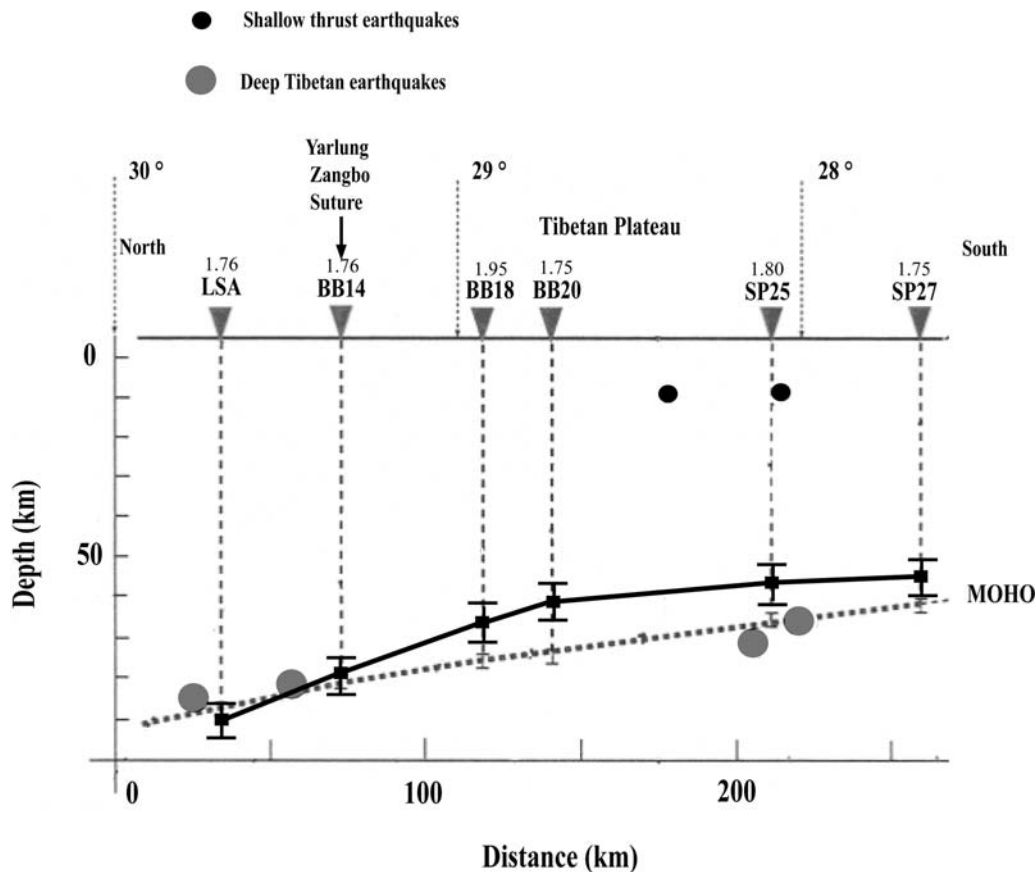


**Figure 8.** A north–south profile of the southern Tibetan Plateau adapted from Mitra *et al.* (2005). The inverted triangles show the locations of the stations used in this article. The vertical dashed lines show the locations of the velocity functions under the individual stations. The solid and dotted lines indicate the variation of the Moho depths from the inversion of the deconvolved vertical components and the Moho depths from inverting receiver functions as obtained by Mitra *et al.* (2005), respectively. The black circles are shallow thrust earthquakes and the gray circles are deep Tibetan earthquakes from Mitra *et al.* (2005). The numbers above the station names are the average crustal  $V_P/V_S$  ratios.

that obtained by the inversion of receiver function data by Mitra *et al.* (2005). The vertical dashed lines show the locations of the velocity profiles beneath each station. The solid bold line indicates the variation of the Moho depths obtained from the inversions of the vertical component data for the  $V_P$  velocities, and the dotted line is the Moho depths obtained from the receiver function inversions of Mitra *et al.* (2005). The black circles are shallow thrust earthquakes, and the gray circles are deep Tibetan earthquakes from Mitra *et al.* (2005) (from their table A1).

In Figure 8, the average crustal  $V_P/V_S$  ratios are shown above each station name. This is based on the crustal  $V_P$  velocities from the inversions of the deconvolved vertical components and the grouped  $V_S$  velocities derived from the receiver function modeling of Mitra *et al.* (2005). With the exception of station BB18, with a somewhat higher  $V_P/V_S$  ratio, the other stations to the north in the Tethyan Himalayas and the southern Lhasa terrane have  $V_P/V_S$  ratios between 1.75 and 1.80, with a mean of 1.77 and a Poisson's ratio of 0.265. The variability could result from noise in the data as well as from lateral heterogeneity in the region with different piercing points at depth for the  $P_s$  and  $PpPp$  phases. The

mean value is comparable to the value obtained by Owens and Zandt (1997) and similar to values shown by Kind *et al.* (2002) for the Tethyan Himalayas and southern Lhasa terrane.

The difference in the Moho depths from this study compared to those of Mitra *et al.* (2005) is primarily between the higher Himalaya to the south and the Zangbo Suture where the structure is most complex. The region sampled by the  $PpPmp$  phase is considerably wider as compared to the  $P_s$  phase used by Mitra *et al.* (2005) for the inversions. This could be a plausible explanation for the variation in the Moho depths obtained from the two methods because depth variability exists within very small distances, which has been previously suggested by Hirn *et al.* (1984) beneath the Nepal Himalaya from deep seismic survey profiles. The earthquake locations beneath station SP25 from Zhu and Helmberger (1996) now lie just below the Moho depths obtained from deconvolved vertical component inversions. However, the deep Tibetan earthquakes near station LSA to the north are still located slightly above the Moho depths obtained from this study.

## Conclusions

The SVA method of Dasgupta and Nowack (2006) has been tested using three-component seismic data in southern Tibet. The SVA deconvolved vertical components were then used to model the *PpPp* reflected phases for *P*-wave velocity structure. The inversion results as shown in Figure 7 for stations LSA and BB14, north of the Zangbo suture in the Tibetan Plateau compare very well with the Moho depths obtained by Mitra *et al.* (2005). The depth of the Moho around this region varies from 80 to 90 km indicating a thick crust, which has also been suggested by other workers. Stations BB18, BB20, SP25, and SP27 lying south of the Zangbo suture show progressively shallower depths of the Moho and also somewhat shallower than the depths obtained by Mitra *et al.* (2005) using receiver function analysis. However, the topography of the Moho in this region is a 3D complex structure, which can lead to these variations of depths for the inversion results of compressional and shear waves. In comparing two 1D velocity models at a given station, similar velocities at the conversion points for the *P* to *S* transmitted conversions and the *P* to *P* reflections are required. This is unlikely in an area with such a complex geometry because the region sampled by the *PpPp* phase is wider than the *Ps* phase and could account for the Moho depth variations from these two approaches. Nonetheless, we were able to constrain the *PpPp* phase on the deconvolved vertical components using the SVA approach and obtain comparable Moho depths as obtained by other workers.

With the exception of station BB18, with a somewhat higher  $V_P/V_S$  ratio, the other stations to the north in the Tethyan Himalayas and the southern Lhasa terrane have  $V_P/V_S$  ratios between 1.75 and 1.80, with a mean of 1.77 and a Poisson's ratio of 0.265. This is similar to the global average for the continental crust (Zandt and Ammon, 1995). The variability could result from noise in the data as well as from lateral heterogeneity in the region with different piercing points at depth for the *Ps* and *PpPp* phases.

## Data and Resources

The data used in this article were from the INDEPTH Phase II Experiment and is available from the Incorporated Research Institutions for Seismology (IRIS) Data Management Center. Key scientific results from INDEPTH II are summarized by Brown *et al.* (1996), Kind *et al.* (1996), Chen *et al.* (1996), and Nelson *et al.* (1996).

## References

- Ammon, C., G. Randall, and G. Zandt (1990). On the nonuniqueness of receiver function inversions, *J. Geophys. Res.* **95**, 15,303–15,318.
- Bostock, M. G. (2004). Green's functions, source signatures, and the normalization of teleseismic wave fields, *J. Geophys. Res.* **109**, B03303, doi 10.1029/2003JB002783.
- Brown, L. D., W. Zhao, K. D. Nelson, M. Hauck, D. Alsdorf, A. Ross, M. Cogan, M. Clark, X. Liu, and J. Che (1996). Bright Spots, structure, and magmatism in southern Tibet from INDEPTH seismic reflection profiling, *Science* **274**, 1688–1690.
- Chen, W. P., and P. Molnar (1981). Constraints on the seismic wave velocity structure beneath the Tibetan Plateau and their tectonic implications, *J. Geophys. Res.* **86**, 5937–5962.
- Chen, W. P., and P. Molnar (1990). Source parameters of earthquakes and intraplate earthquakes and their implications for the thermal and mechanical properties of the lithosphere, *J. Geophys. Res.* **95**, 12,527–12,552.
- Chen, W. P., and Z. Yang (2004). Earthquakes beneath the Himalayas and Tibet: Evidence for strong lithospheric mantle, *Science* **304**, 1949–1952.
- Chen, L., J. R. Booker, A. G. Jones, W. Nong, M. J. Unsworth, W. Wei, and H. Tan (1996). Electrically conductive crust in southern Tibet from INDEPTH magnetotelluric surveying, *Science* **274**, 1694–1696.
- Christensen, N. I. (1996). Poisson's ratio and crustal seismology, *J. Geophys. Res.* **101**, 3139–3156.
- Dasgupta, S., and R. L. Nowack (2006). Deconvolution of three-component teleseismic *P* waves using the autocorrelation of the *P* to *SV* scattered waves, *Bull. Seismol. Soc. Am.* **96**, 1827–1835.
- Hearn, T. M., S. Wang, J. Ni, Z. Xu, Y. Yu, and X. Zhang (2004). Uppermost mantle velocities beneath China and surrounding regions, *J. Geophys. Res.* **109**, B11301, doi 10.1029/2003JB002874.
- Hirn, A., J. Lepine, G. Jobert, M. Sapin, G. Wittlinger, X. Xin, G. Yuan, W. Jing, T. Wen, X. S. Bai, M. R. Pandey, and J. Tater (1984). Crustal structure and variability of the Himalayan border of Tibet, *Nature* **307**, 23–25.
- Jackson, J. (2002). Strength of the continental lithosphere: Time to abandon the jelly sandwich?, *GSA Today* **12**, 4–10.
- Kind, R., J. Ni, W. Zhao, J. Wu, X. Yuan, L. Zhao, E. Sandvol, C. Reese, J. Nabelek, and T. Hearn (1996). Evidence from earthquake data for a partially molten crustal layer in Tibet, *Science* **274**, 1692–1694.
- Kind, R., X. Yuan, J. Saul, D. Nelson, S. V. Sobolev, J. Mechie, W. Zhao, G. Kosarev, J. Ni, U. Achauer, and M. Jiang (2002). Seismic images of crust and upper mantle beneath Tibet: Evidence for Eurasian subduction, *Science* **298**, 1219–1221.
- Li, S., and W. D. Mooney (1997). Crustal structure of China from deep seismic sounding profiles, *Tectonophysics* **288**, 105–113.
- Li, S., W. D. Mooney, and J. Fan (2006). Crustal structure of mainland China from deep seismic sounding data, *Tectonophysics* **420**, 239–252.
- Liang, C., and X. Song (2006). A low velocity belt beneath northern and eastern Tibetan Plateau from Pn tomography, *Geophys. Res. Lett.* **33**, L22306, doi 10.1029/2006GL027926.
- Mitra, S., K. Priestley, A. Kr. Bhattacharya, and V. K. Gaur (2005). Crustal structure and earthquake focal depths beneath northeastern India and southern Tibet, *Geophys. J. Int.* **160**, 227–248.
- Monsalve, G., A. Sheehan, V. Schulte-Pelkum, S. Rajaura, M. R. Pandey, and F. Wu (2006). Seismicity and one-dimensional velocity structure of the Himalayan collision zone: Earthquakes in the crust and upper mantle, *J. Geophys. Res.* **111**, B10301, doi 10.1029/2005JB004062.
- Nelson, K. D., W. J. Zhao, L. D. Brown, J. Kuo, J. K. Che, X. W. Liu, S. L. Klempner, Y. Makovsky, R. Meissner, J. Mechie, R. Kind, F. Wenzel, J. Ni, J. Nabelek, L. S. Chen, H. D. Tan, W. B. Wei, A. G. Jones, J. Booker, M. Unsworth, W. S. F. Kidd, M. Hauck, D. Alsdorf, A. Ross, M. Cogan, C. D. Wu, E. Sandvol, and M. Edwards (1996). Partially molten middle crust beneath southern Tibet: Synthesis of project INDEPTH results, *Science* **274**, 1684–1688.
- Oppenheim, A. V., and R. W. Schaffer (1975). *Digital Signal Processing*, Prentice-Hall, Englewood Cliffs.
- Owens, T. J., and G. Zandt (1997). Implications of crustal property variations for models of Tibetan plateau evolution, *Nature* **387**, 37–43.
- Rai, S. S., K. Priestley, K. Suryaprakasham, D. Sriganesh, V. K. Gaur, and D. Zu (2003). Crustal shear velocity structure of the south Indian shield, *J. Geophys. Res.* **108**, no. B2, 2088, doi 10.1029/2002JB001776.
- Robinson, E. A., and O. M. Osman (1996). *Deconvolution 2*, Geophysics reprint series No. 17, Society of Exploration Geophysicists, Tulsa, Oklahoma.

- Rodgers, A. J., and S. Y. Schwartz (1997). Low crustal velocities and mantle lithospheric variations in southern Tibet from regional *Pnl* waveforms, *Geophys. Res. Lett.* **24**, 9–12.
- Schulte-Pelkum, V., G. Monsalve, A. Sheehan, M. R. Pandey, S. Sapkota, and R. Bilham (2005). Imaging the Indian subcontinent beneath the Himalaya, *Nature* **435**, 1222–1225.
- Sun, Y., and M. N. Toksoz (2006). Crustal structure of China and surrounding regions from *P* wave travel time tomography, *J. Geophys. Res.* **111**, B03310, doi 10.1029/2005JB003962.
- Tarantola, A. (1987). *Inverse Problem Theory: Methods for Data Fitting and Model Parameter Estimation*, Elsevier, Amsterdam.
- Tarantola, A. (2005). *Inverse Problem Theory and Model Parameter Estimation*, SIAM, Philadelphia.
- Webster, G. M. (Editor), (1978). *Deconvolution*, Geophysics reprint series No. 1, Society of Exploration Geophysicists, Tulsa, Oklahoma.
- Yuan, X. H., J. Ni, R. Kind, J. Mechie, and E. Sandvol (1997). Lithospheric and upper mantle structure of southern Tibet from a seismological passive source experiment, *J. Geophys. Res.* **102**, 27,491–27,500.
- Zandt, G., and G. J. Ammon (1995). Continental crust composition constrained by measurements of crustal Poisson's ratio, *Nature* **374**, 152–154.
- Zhu, L., and D. V. Helmberger (1996). Intermediate depth earthquakes beneath the India–Tibet collision zone, *Geophys. Res. Lett.* **23**, 435–438.

## Appendix

### The SVA Technique

This appendix provides a brief overview of the SVA technique. A more complete description of the method, along with examples, can be found in Dasgupta and Nowack (2006). Assume first that the seismic *P* phases oriented in the direction of the incident teleseismic *P* wave are made up of the direct *P* arrival represented by a delta function followed by random *P* to *P* scattering coefficients,  $R_{P-P}(t)$ . Thus,

$$R_P(t) = \delta(t) + R_{P-P}(t). \quad (\text{A1})$$

The scattered *SV* phases oriented perpendicular to the direction of the direct *P* wave includes only *P* to *SV* scattering coefficients  $R_{P-SV}(t)$ . The rotated and transformed *P* and *SV* components are the result of the scattering time series  $R_P(t)$  and  $R_{P-SV}(t)$  being convolved with the source wavelet as,

$$P(t) = S(t) * \{\delta(t) + R_{P-P}(t)\}, \quad (\text{A2})$$

$$SV(t) = S(t) * R_{P-SV}(t), \quad (\text{A3})$$

where  $*$  indicates convolution.

The autocorrelation function of the *SV* component will be approximately equal to the autocorrelation function of the source wavelet if the scattering coefficients are random and white. Thus,

$$SV(t) * SV(-t) = \{S(t) * S(-t)\} * \{R_{P-SV}(t) * R_{P-SV}(-t)\} \sim S(t) * S(-t), \quad (\text{A4})$$

where  $\{R_{P-SV}(t) * R_{P-SV}(-t)\} \sim \delta(t)$  for random and white *P* to *SV* scattering coefficients. This is similar to the assumption made for the deconvolution of reflection seismograms in exploration seismology where *P* to *P* scattering coefficients are assumed to be random and white (Webster, 1978; Robinson and Osman, 1996). The Fourier transform of the autocorrelation of the source wavelet is its power spectrum. Thus, the Fourier transform of  $S(t) * S(-t)$  is  $|S(\omega)|^2$  and the Fourier transform of  $R_{P-SV}(t) * R_{P-SV}(-t)$  is approximately 1 for a random and white scattering series  $R_{P-SV}(t)$ .

To obtain the full source wavelet from the power spectrum, the phase spectrum is required. For a minimum phase signal, the log of the power spectrum and the phase spectrum form a Hilbert transform pair (Oppenheim and Schaffer, 1975). We can therefore construct a minimum phase source wavelet from the power spectrum and use it for the deconvolution. However, an earthquake source time function is not, in general, minimum phase. But the unrotated seismic data can be processed to be minimum phase, and this processed data can be deconvolved with the estimated minimum phase source wavelet from the SVA function. This assumes that the direct *P* is larger than the scattered waves on these components.

For the rotated *P*(*t*) component, the direct wave is included along with the *P* to *P* scattered phases. Following Bo-stock (2004), we assume that  $\{\delta(t) + R_{P-P}(t)\}$  is minimum phase for near vertically scattered waves from an incident teleseismic wave. Therefore, the scattered waves will all be smaller in amplitude than the direct wave for this component. For this case, the processed minimum phase version of *P*(*t*),  $P_{MP}(t)$  is just the minimum phase version of the source wavelet  $S_{MP}(t)$  convolved with  $\{\delta(t) + R_{P-P}(t)\}$ . Because the minimum phase source wavelet  $S_{MP}(t)$  can be obtained from the autocorrelation of the *SV* component of the data, we can deconvolve  $P_{MP}(t)$  by  $S_{MP}(t)$  to find the scattering series  $R_{P-P}(t)$ . To find  $R_{P-SV}(t)$  we rotate to directions in a cone about the direct *P*-wave direction and then compute the minimum phase signals. These are then rotated back to the vertical and radial components and deconvolved with the minimum phase wavelet  $S_{MP}(t)$ . Additional stabilization of the results can be obtained by stacking over different events or by smoothing or stacking the power spectra of the initial autocorrelations.

Department of Earth and Atmospheric Sciences  
550 Stadium Mall Drive  
Purdue University  
West Lafayette, Indiana 47907  
(S.D., R.L.N.)

Department of Geology and Geophysics  
Indian Institute of Technology  
Kharagpur, West Bengal-721302 India  
(S.M.)